# Analysis of the clustering of inertial particles in turbulent flows

Mahdi Esmaily-Moghadam* and Ali Mani
*Center for Turbulence Research, Stanford University, Stanford, California, USA*
(Received 12 January 2016; revised manuscript received 12 February 2016; published 20 December 2016)

An asymptotic solution is derived for the motion of inertial particles exposed to Stokes drag in an unsteady random flow. This solution provides an estimate for the sum of Lyapunov exponents as a function of the Stokes number and Lagrangian strain- and rotation-rate autocovariance functions. The sum of exponents in a Lagrangian framework is the rate of contraction of clouds of particles, and in an Eulerian framework, it is the concentration-weighted divergence of the particle velocity field. Previous literature offers an estimate of the divergence of the particle velocity field, which is applicable only in the limit of small Stokes numbers [Robinson, Comm. Pure Appl. Math. **9**, 69 (1956) and Maxey, J. Fluid Mech. **174**, 441 (1987)] (R-M). In addition to reproducing R-M at this limit, our analysis provides a first-order correction to R-M at larger Stokes numbers. Our analysis is validated by a directly computed rate of contraction of clouds of particles from simulations of particles in homogeneous isotropic turbulence over a broad range of Stokes numbers. Our analysis and R-M predictions agree well with the direct computations at the limit of small Stokes numbers. At large Stokes numbers, in contrast to R-M, our model predictions remain bounded. In spite of an improvement over R-M, our analysis fails to predict the expansion of high Stokes clouds observed in the direct computations. Consistent with the general trend of particle segregation versus Stokes number, our analysis shows a maximum rate of contraction at an intermediate Stokes number of $O(1)$ and minimal rates of contraction at small and large Stokes numbers.

DOI: 10.1103/PhysRevFluids.1.084202

## I. INTRODUCTION

Inertial particles interacting with a spatially varying flow form regions of high concentration. This is known as particle clustering [1], segregation [2], or preferential concentration [3]. The prevalence of particle-laden flow in areas of physics and engineering has inspired decades of research with applications ranging from planet and cloud formation to combustion and pharmaceutical applications [4,5].

These studies have established that clustering occurs when particles, characterized by their Stokes numbers (St), have a response time of order unity. At significantly higher Stokes numbers particles follow a ballistic trajectory that is independent of the flow. Particles with $\mathrm{St} \ll 1$ follow the fluid as tracers with a minimal relative motion that is essential to the formation of clusters. Various approaches have been adopted to relate clustering to the background flow and Stokes number. Experimental studies [4,6–9] and numerical simulations [2,10–16] have shown that Stokes numbers of order unity based on the Kolmogorov time scale are associated with the strongest clustering regime.

Under a particular set of conditions, such as low particle Reynolds and Knudsen numbers, high particle-to-fluid density ratio, absence of body force, negligible finite size effects, negligible particle-particle and particle-wall interactions, and low mass loading ratio, particle motion is well described in these systems by the Stokes equation

$$\ddot{X}_i = \tau^{-1}(u_i - \dot{X}_i), \tag{1}$$

in which $\boldsymbol{X}(t)$ is the position of a particle, $t$ is time, $(\dot{\bullet}) \equiv \mathrm{d}(\bullet)/dt$, $\boldsymbol{u}(\boldsymbol{X},t)$ is the fluid velocity, and $\tau$ is the particle relaxation time. Although Eq. (1) seems a simple ordinary differential equation, it exhibits a nonlinear chaotic behavior due to the dependence of its source term on $\boldsymbol{X}$ [17]. For systems

*Corresponding author: mesmaily@stanford.edu

 

in which the assumptions associated with Eq. (1) are not completely valid, the Stokes number retains a large influence on clustering with a trend that is similar to the dynamics predicted by this simplified equation. Therefore, we consider Eq. (1) as the starting point to investigate the underlying physics of clustering at a more fundamental level and explicate the role of Stokes number in this process.

Multiple indices have been introduced in the literature for characterization of particle clustering [18]. Here we consider two classes of indices and describe their relationship. The first index is defined based on the rate at which nearby particles separate or approach each other. In other words, provided two particles at an initial infinitesimal distance $\|\boldsymbol{r}(0)\|$, they converge or diverge exponentially as

$$\|\boldsymbol{r}(t)\| = \|\boldsymbol{r}(0)\|e^{\lambda t}. \tag{2}$$

$\lambda$ is called the finite-time Lyapunov exponent and converges to the Lyapunov exponent in an ergodic system as $t \to \infty$ [19]. Exponents much smaller than zero are indicative of a strong clustering regime. As discussed in detail in the following section, there are three exponents ($\lambda_1$, $\lambda_2$, and $\lambda_3$) in a three-dimensional flow that determine the rate of expansion and contraction of a cloud of particles in three orthogonal directions. Hence, these exponents are directly related to the rate of contraction of a cloud, which as discussed in Ref. [20] is connected to the particle number density and provide a measure of clustering.

The second index for characterization of clustering is based on the statistics of particle concentration field, which is experimentally measurable and less mathematically abstract. At the limit of small Stokes numbers, the particle concentration field is a fractal [1]. Analytical relationships are established for different order statistics of a fractal and employed in this context for characterization of clustering [21]. For instance, the scaling exponent $\zeta(n)$ obtained from $m^n = D^\zeta$, in which $m(D)$ is the average mass of particles inside an infinitesimal sphere with diameter $D$, varies depending on the level of clustering. For example, clustering of randomly distributed particles in three dimensions toward a two-dimensional (2D) manifold reduces $\zeta$ from $3n$ to $2n$. For a fractal concentration field, $\zeta$ is directly related to the Lyapunov exponents and as a result to the first index described above [22,23]. Hence, the Lyapunov exponents provide an estimate for a more experimentally accessible clustering index and are of prime importance for characterization of particle clustering.

The divergence of the particle velocity field is equal to the sum of the Lyapunov exponents (i.e. $\lambda_1 + \lambda_2 + \lambda_3$), and computing it relates both indices described above to the background flow. At the limit of small Stokes numbers, an expression has been derived by Robinson [24] and Maxey [25] for the divergence of particle velocity field by taking the divergence of Eq. (1) under the assumptions $\ddot{\boldsymbol{X}} \approx \mathrm{D}\boldsymbol{u}/\mathrm{D}t$ and $\boldsymbol{\nabla} \cdot \boldsymbol{u} = 0$. This expression, which we consider for benchmarking our analysis and denote by R-M, is

$$\overline{\boldsymbol{\nabla} \cdot \dot{\boldsymbol{X}}} \approx -\tau \overline{\boldsymbol{\nabla} \cdot (\boldsymbol{u} \cdot \boldsymbol{\nabla} \boldsymbol{u})} = \tau \overline{(\|\boldsymbol{\Omega}\|^2 - \|\boldsymbol{S}\|^2)} \equiv \tau\, Q, \tag{3}$$

in which $\boldsymbol{\Omega}$ and $\boldsymbol{S}$ are the fluid rotation- and strain-rate tensors, respectively, and the overline denotes averaging in time over the trajectory of a particle. Note that the difference between the norm of these two tensors (here defined as $Q$) corresponds to the second invariant of the velocity gradient tensor and half of the $Q$ criterion, which is a scalar function employed for identification of vortices in turbulent flows [26,27]. The R-M expression explains that the most hospitable zones for clustering are those with high strain and low rotation rate that are conducive to the highest rate of contraction. Although this relation provides information about both indices through the sum of Lyapunov exponents, it is linearly proportional to $\tau$ and fails to predict the nonmonotonic behavior of particle clustering versus the Stokes number.

The primary objective of this study is finding a correction to R-M that not only reproduces it at the limit of small Stokes number [the regime that Eq. (3) applies to] but also is applicable to a wider range of Stokes numbers. With this motivation in mind, in what follows, an asymptotic solution is derived from Eq. (1) that quantifies the sum of Lyapunov exponents associated with inertial particle pairs. This solution expresses the sum of exponents as a function of Stokes number and background flow statistics and hence can be related to both indices described above.

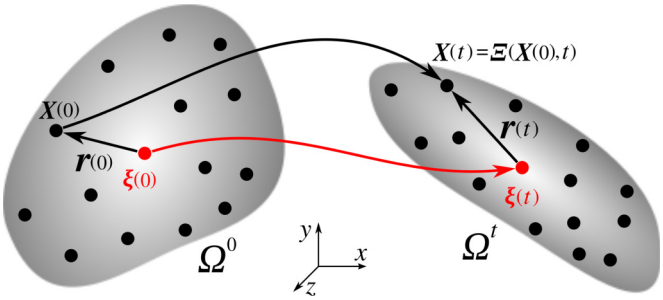


FIG. 1. Schematic of a cloud of particles, $\Omega^t$, defined as an infinitesimal 3D manifold occupied by a collection of particles. This cloud, which undergoes deformation characterized by $\boldsymbol{\Xi}$, may expand or contract toward a central point $\boldsymbol{\xi}$.

In what follows, we consider a general representation of flow with oscillatory modes of strain and rotation acting simultaneously over all possible frequencies. We derive an eigenvalue problem with its eigenvalues and eigenvectors representing magnitude and directions of contractions, respectively. We show the dependence of this eigenvalue problem on the Stokes number, explaining how a particle may filter or resonate with different frequencies. We perform a detailed analysis of the Lagrangian autocovariance functions, which are the input to our analysis, and benchmark their response with a set of canonical flows. Finally, we present a validation of our analysis through a quantitative comparison against direct numerical simulation (DNS) of particle-laden homogeneous isotropic turbulent (HIT) flow.

## II. ANALYTICAL DERIVATION

As the starting point, we consider a volume occupied by a collection of nearby particles, which we call a cloud. This cloud is initially denoted by $\Omega^0$ and evolves over time with $\boldsymbol{\Xi} : \Omega^0 \to \Omega^t$ (Fig. 1). By taking function $\boldsymbol{\Xi}$ to satisfy Eq. (1), $\Omega^t = \{\boldsymbol{X}(t) \mid \boldsymbol{X}(t) = \boldsymbol{\Xi}(\boldsymbol{X}(0),t), \boldsymbol{X}(0) \in \Omega^0\}$. By following $\Omega^t$, the problem is formulated on a reference frame that moves with the cloud.

Denoting the central point of the cloud by $\boldsymbol{\xi}$, relative motion of a particle located at $\boldsymbol{X} \in \Omega^t$ to the central point is $\boldsymbol{r}(t) = \boldsymbol{X}(t) - \boldsymbol{\xi}(t)$ (Fig. 1). Substituting this relation in Eq. (1) gives

$$\tau(\ddot{\xi}_i + \ddot{r}_i) + \dot{\xi}_i + \dot{r}_i = u_i(\boldsymbol{\xi} + \boldsymbol{r}, t). \tag{4}$$

By bounding the size of the cloud to be much less than the Kolmogorov length scale $\eta$, we ensure that the size of the cloud is always less than the inertial length, and as a result particles within the cloud experience a smooth linear velocity field. Hence, from the Taylor series expansion,

$$u_i(\boldsymbol{\xi} + \boldsymbol{r}, t) = u_i(\boldsymbol{\xi}, t) + u_{i,j}(\boldsymbol{\xi}, t) r_j + O(\|\boldsymbol{r}\|^2), \tag{5}$$

in which $(\bullet)_{,i} \equiv \partial(\bullet)/\partial x_i$. Neglecting the higher order terms in Eq. (5) and using $\tau\ddot{\xi}_i + \dot{\xi}_i = u_i(\boldsymbol{\xi}, t)$ to simplify Eq. (4) leads to

$$\tau\ddot{r}_i + \dot{r}_i = u_{i,j}(\boldsymbol{\xi}, t) r_j, \tag{6}$$

which is an exact linearized form of Eq. (1), provided $\|\boldsymbol{r}\|$ is sufficiently small. Here we have derived Eq. (6) from Eq. (1) in several steps to build physical intuition. This equation can also be obtained by taking the derivative of Eq. (1) with respect to $\boldsymbol{X}(0)$ as shown in Ref. [16].

Next, we express fluid velocity in a continuous Lagrangian Fourier space that follows the cloud:

$$u_i(\boldsymbol{\xi}, t) = \sum_{\omega} \tilde{u}_i(\omega) e^{\hat{i}\omega t}, \tag{7}$$

in which $\omega = (-\infty, \infty)$. Since finding $\boldsymbol{r}$ for an individual cloud is of interest, dependence of $\tilde{\boldsymbol{u}}$ on $\boldsymbol{\xi}$ is dropped from Eq. (7). From Eqs. (7) and (6),

$$\tau \ddot{r}_i + \dot{r}_i = \sum_{\omega} \tilde{u}_{i,j}(\omega) r_j e^{\hat{i}\omega t}. \tag{8}$$

These three ordinary differential equations relate particle motion to the harmonics of the velocity gradient tensor sampled along the trajectory of the cloud. One significance of this relation is that the fluid velocity gradient is characterized by the Kolmogorov scale and thus explains our earlier use of Kolmogorov units. The appearance of the velocity gradient tensor in Eq. (8) does not imply that it captures only a subset of existing scales of the flow. $u_{i,j}$ is a general function of time and accounts for the full turbulent spectrum, including the longer time scales of the inertial range. Additionally, due to the turbulence intermittency $\tilde{u}_{i,j}$ cannot be represented as a unique set of harmonic functions. However, as shown later in this section, it is still possible to derive a generic solution for the rate of contraction that converges statistically with sufficient sampling.

Denoting the volume of the cloud $\Omega^t$ by $V(\Omega^t)$, the finite-time rate of contraction $\mathcal{C}^t$ is defined such that

$$V(\Omega^t) = V(\Omega^0) \exp(\mathcal{C}^t t). \tag{9}$$

Based on Eq. (9), we define a time-independent rate of contraction as

$$\mathcal{C} \equiv \lim_{t \to \infty} \mathcal{C}^t. \tag{10}$$

With these definitions the cloud might rotate or even expand in a particular direction, but it contracts as long as the number density within the cloud increases. To quantify $\mathcal{C}$, we search for an asymptotic solution to Eq. (8) with a form of

$$r_i = e^{\lambda t} \sum_{\omega} A_i(\omega) e^{\hat{i}\omega t}, \tag{11}$$

in which $\lambda$ and $A_i$ are the free eigenvalues and eigenfunctions to be determined. Considering the upper bound on $\|\boldsymbol{r}\|$, $\lambda$ at $t \to \infty$ is the Lyapunov exponent associated with particle pairs at $\boldsymbol{\xi}$ and $\boldsymbol{\xi} + \boldsymbol{r}$. The form of the solution in Eq. (11) allows for oscillation over all possible frequencies, $\omega$, as well as contraction or expansion characterized by $\lambda$. Specifically, we seek contractions and expansions that persist over time scales longer than particle relaxation time, and thus regimes with

$$|\lambda \tau| \ll 1 \tag{12}$$

are of particular interest.

Next, we expand our formulation at $|\omega| < |\lambda|$ and $|\omega| > |\lambda|$ and simplify it using Eq. (12) to obtain a $3 \times 3$ eigenvalue problem. For the sake of brevity, we use short-hand notations $\boldsymbol{A}^m \equiv \boldsymbol{A}(\omega^m)$ and $\tilde{\boldsymbol{u}}^{m-n} \equiv \tilde{\boldsymbol{u}}(\omega^m - \omega^n)$. Substituting Eq. (11) in Eq. (8) yields

$$\sum_{\omega^m} [\tau(\hat{i}\omega^m + \lambda)^2 + \hat{i}\omega^m + \lambda] A_i^m e^{\hat{i}\omega^m t} = \sum_{\omega^l} \sum_{\omega^n} \tilde{u}_{i,j}^l A_j^n e^{\hat{i}(\omega^l + \omega^n)t}. \tag{13}$$

Since summations are calculated over infinite intervals, we take $\omega^l = \omega^m - \omega^n$ to simplify Eq. (13) to

$$\sum_{\omega^m} [\tau(\hat{i}\omega^m + \lambda)^2 + \hat{i}\omega^m + \lambda] A_i^m e^{\hat{i}\omega^m t} = \sum_{\omega^m} \sum_{\omega^n} \tilde{u}_{i,j}^{m-n} A_j^n e^{\hat{i}\omega^m t}, \tag{14}$$

which must hold at any $t$. This is achieved by ensuring

$$[\tau(\hat{i}\omega^m + \lambda)^2 + \hat{i}\omega^m + \lambda] A_i^m = \sum_{\omega^n} \tilde{u}_{i,j}^{m-n} A_j^n \tag{15}$$

is satisfied for any $\omega^m$. In the following, we enforce this condition separately for small and large $\omega^m$.

Approximating Eq. (15) for $|\omega^m| < |\lambda|$ yields

$$(\tau\lambda + 1)\lambda A_i^m \approx \sum_{\omega^n} \tilde{u}_{i,j}^{m-n} A_j^n, \tag{16}$$

and for $|\omega^m| > |\lambda|$

$$[-\tau(\omega^m)^2 + \hat{\imath}\omega^m] A_i^m \approx \sum_{\omega^n} \tilde{u}_{i,j}^{m-n} A_j^n. \tag{17}$$

Note that $\omega^n$ inside the summation in Eqs. (16) and (17) is not limited to small or large frequencies and covers the full spectrum of $\tilde{u}_{i,j}$. Rearranging Eq. (17) gives

$$A_k^n = -\sum_{\omega^l} \frac{\tau + \hat{\imath}/\omega^n}{1 + (\tau\omega^n)^2} \tilde{u}_{k,j}^{n-l} A_j^l \tag{18}$$

for $|\omega^n| > |\lambda|$. The first term in Eq. (16) can be neglected since $|\tau\lambda| \ll 1$ [see Eq. (12)]. Therefore, substituting Eq. (18) in Eq. (16) yields

$$\lambda A_i^m = -\sum_{|\omega^n|>|\lambda|} \sum_{\omega^l} \frac{\tau + \hat{\imath}/\omega^n}{1 + (\tau\omega^n)^2} \tilde{u}_{i,k}^{m-n} \tilde{u}_{k,j}^{n-l} A_j^l + \sum_{|\omega^n|<|\lambda|} \sum_{\omega^l} \frac{1}{\lambda} \tilde{u}_{i,k}^{m-n} \tilde{u}_{k,j}^{n-l} A_j^l \tag{19}$$

for $|\omega^m| < |\lambda|$. Since the aim of this analysis is obtaining ensemble-averaged quantities over long periods, we neglect the terms with $l \neq m$ in Eq. (19) ($\tilde{u}_{i,k}^{m-n}$ and $\tilde{u}_{i,k}^{n-l}$ are uncorrelated for $l \neq m$). Hence

$$\lambda A_i^m = -\sum_{|\omega^n|>|\lambda|} \frac{\tau + \hat{\imath}/\omega^n}{1 + (\tau\omega^n)^2} \tilde{u}_{i,k}^{m-n} \tilde{u}_{k,j}^{n-m} A_j^m + \sum_{|\omega^n|<|\lambda|} \frac{1}{\lambda} \tilde{u}_{i,k}^{m-n} \tilde{u}_{k,j}^{n-m} A_j^m \tag{20}$$

for $|\omega^m| < |\lambda|$. The velocity gradients in Eq. (20) are a function of $|\omega^n - \omega^m|$. Since in the first summation $|\omega^n| > |\lambda|$ and $|\omega^m| < |\lambda|$, we neglect $\omega^m$ in this summation. Additionally, the second summation is summed over a short range compared to the physical infinity, *viz.,* of order $\tau_\eta^{-1}$. Hence, we neglect this term in comparison with the first summation, which is summed over a much wider range of frequencies. Our numerical results show $|\tau_\eta\lambda| \ll 1$. As a result Eq. (20) reduces to

$$\lambda A_i^m = -\sum_{|\omega^n|>|\lambda|} \frac{\tau + \hat{\imath}/\omega^n}{1 + (\tau\omega^n)^2} \tilde{u}_{i,k}^{-n} \tilde{u}_{k,j}^{n} A_j^m \tag{21}$$

for $|\omega^m| < |\lambda|$. In Eq. (21), the term with $\hat{\imath}/\omega^n$ is an odd function of $\omega^n$ and is canceled. Additionally, taking $\omega = \omega^n$ yields

$$\lambda A_i^m = -\left[\sum_{|\omega|>|\lambda|} \frac{\tau}{1 + (\tau\omega)^2} \tilde{u}_{i,k}^{*} \tilde{u}_{k,j}\right] A_j^m \tag{22}$$

for $|\omega^m| < |\lambda|$, in which $\tilde{\boldsymbol{u}}^*$ is the complex conjugate of $\tilde{\boldsymbol{u}}$ and is equal to $\tilde{\boldsymbol{u}}(-\omega)$, since $\boldsymbol{u} \in \mathbb{R}^3$.

The summation in Eq. (22) includes only $|\omega| > |\lambda|$, and hence its computation requires a prior knowledge of $\lambda$. To remove this dependence, we extend the summation to all frequencies by including $|\omega| < |\lambda|$ in this summation. This change in summation bounds is in accordance with our earlier assumption in which the contribution of $|\omega| < |\lambda|$ is negligible compared to $|\omega| > |\lambda|$. The contribution of these small frequencies is of the same order as the second summation in Eq. (20) that was neglected earlier. Therefore, this approximation remains within the leading order of accuracy of this analysis. Including $|\omega| < |\lambda|$ in Eq. (22) leads to

$$\lambda A_i^m = -\left[\sum_{\omega} \frac{\tau}{1 + (\tau\omega)^2} \tilde{u}_{i,k}^{*} \tilde{u}_{k,j}\right] A_j^m \tag{23}$$

for $|\omega^m| < |\lambda|$. Note that the expression inside the bracket is not a function of $\omega^m$, indicating that $\lambda$ is the same at small frequencies. Therefore, Eq. (23) can be written as

$$\boldsymbol{\psi} \boldsymbol{A}^0 = \lambda \boldsymbol{A}^0, \tag{24}$$

in which $\boldsymbol{A}^0$ is the displacement vector associated with the low-frequency oscillations, i.e., $|\omega^m| < |\lambda|$, and

$$\psi_{ij} \equiv -\sum_{\omega} \frac{\tau}{1+(\tau\omega)^2} \tilde{u}^*_{i,k} \tilde{u}_{k,j}. \tag{25}$$

The three eigenvectors of $\boldsymbol{\psi}$ represent the principal directions at which the cloud experiences pure contraction or expansion. The eigenvalues associated with each direction represent the rate of contraction [real($\lambda$) < 0] or expansion [real($\lambda$) > 0]. Numerical investigation shows that generally one of the eigenvalues has a positive and one has a negative real part, hence most clouds expand and contract at the same time, which is consistent with previous reports [13]. The imaginary part of each eigenvalue accounts for the mean rotation.

While the instantaneous rate of expansion or contraction of a cloud is subject to oscillations due to the turbulence intermittency, the long-term change of $V(\Omega^t)$ is solely controlled by $\lambda$ and can be computed from the product of contraction or expansion factors in the principal directions as

$$V(\Omega^t) = V(\Omega^0) \exp(\Lambda_{ii} t) \quad | \; t \to \infty. \tag{26}$$

In this relation, $\boldsymbol{\Lambda}$ is the eigenvalue matrix of $\boldsymbol{\psi}$, hence $\Lambda_{ii}$ is the sum of three Lyapunov exponents $\lambda$. Considering our earlier definition of clustering index, Eq. (26) provides $\Lambda_{ii}$ as the measure of contraction rate for a single cloud of particles. Given that the trace is invariant, $\Lambda_{ii}$ can be directly computed from $\psi_{ii}$. Hence from Eqs. (10) and (26),

$$\mathcal{C} \approx \Lambda_{ii} = \psi_{ii} = -\sum_{\omega} \frac{\tau}{1+(\tau\omega)^2} \tilde{u}^*_{i,j} \tilde{u}_{j,i}. \tag{27}$$

Using the convolution theorem and $\tilde{u}^*_{i,j}\tilde{u}_{j,i} = \tilde{S}^*_{ij}\tilde{S}_{ij} - \tilde{\Omega}^*_{ij}\tilde{\Omega}_{ij}$, Eq. (27) can be expressed in terms of a continuous integral as

$$\mathcal{C}(\tau) = \int_{-\infty}^{\infty} \frac{\tau \tilde{\rho}^{\mathrm{Q}}(\omega)}{1+(\tau\omega)^2} \, d\omega, \tag{28}$$

in which $\tilde{\rho}^{\mathrm{Q}}$ represents the Fourier transform of the autocovariance function $\rho^{\mathrm{Q}}$ defined as

$$\rho^{\mathrm{Q}}(t) \equiv \rho^{\Omega} - \rho^{\mathrm{S}} \equiv \overline{\Omega_{ij}(t')\Omega_{ij}(t'+t)} - \overline{S_{ij}(t')S_{ij}(t'+t)} \tag{29}$$

with overlines denoting Lagrangian averaging over $t'$. Defining

$$\begin{bmatrix} \rho^{\mathrm{I}}(t) \\ \rho^{\mathrm{II}}(t) \\ \rho^{\mathrm{III}}(t) \end{bmatrix} \equiv \begin{bmatrix} \overline{u_{1,1}(t')u_{1,1}(t'+t)} \\ \overline{u_{1,2}(t')u_{1,2}(t'+t)} \\ \overline{u_{1,2}(t')u_{2,1}(t'+t)} \end{bmatrix} \tag{30}$$

for homogeneous and isotropic turbulence, it can be shown that

$$\begin{bmatrix} \rho^{\Omega}(t) \\ \rho^{\mathrm{S}}(t) \\ \rho^{\mathrm{Q}}(t) \end{bmatrix} = 3 \begin{bmatrix} \rho^{\mathrm{II}} - \rho^{\mathrm{III}} \\ \rho^{\mathrm{I}} + \rho^{\mathrm{II}} + \rho^{\mathrm{III}} \\ -\rho^{\mathrm{I}} - 2\rho^{\mathrm{III}} \end{bmatrix}. \tag{31}$$

We will analyze the behavior of these functions in the next section for HIT flow. Since these autocovariance functions are computed along the trajectory of a cloud, they are different from the Eulerian quantities and thus dependent on $\tau$.

Interestingly in the limit of $\mathrm{St} = \tau/\tau_\eta \ll 1$, in which $\tau_\eta$ is the Kolmogorov time scale of the flow, Eq. (28) reduces to

$$\mathcal{C} = \tau \int_{-\infty}^{\infty} \tilde{\rho}^{\mathrm{Q}}\, d\omega = \tau \rho^{\mathrm{Q}}(0) = \tau \overline{(\|\boldsymbol{\Omega}\|^2 - \|\boldsymbol{S}\|^2)} = \tau\, Q, \tag{32}$$

which is identical to R-M expression in Eq. (3). Note that R-M is validated in the limit of $\mathrm{St} < O(1)$, showing its close connection with particle clustering [28,29]. Here using an entirely different approach, we derived a more general expression that targets a wider range of Stokes numbers. Among all flow parameters, this relation depends only on the second invariant of the velocity gradient tensor, confirming the dominant role of viscous scales on producing fluctuation in the particle concentration field [30].

Equation (28) is the most important result of this analysis, which at first glance predicts the maximum rate of contraction $\mathcal{C}$ at intermediate $\tau$ when $\tilde{\rho}^{\mathrm{Q}} < 0$. Additionally, neglecting the dependence of $\tilde{\rho}^{\mathrm{Q}}$ on $\tau$, it predicts the decay of $\mathcal{C}$ for $\tau \to 0$ or $\tau \to \infty$ proportional and inversely proportional to $\tau$, respectively. Furthermore, the fact that the product of $\tau$ and $\omega$ appeared in the denominator of Eq. (28) explains the unresponsiveness of larger particles to the fast oscillations of small flow features.

## III. DIRECT NUMERICAL SIMULATIONS

In this section, we describe the direct numerical simulations that were performed to quantify and verify the analytical results of Sec. II. In particular, we discuss two aspects of these simulations that are critical for a correct assessment of those results. These aspects, although generic and not specific to the present analysis, are essential for reproduction of the reported results and, thus, are discussed for the sake of completeness.

We consider a triply periodic homogeneous isotropic turbulence as the background flow. To simplify collecting statistics over extended periods, we generate a stationary turbulence by continuously injecting energy into the flow via a linear forcing term that is proportional to the velocity [31]. Hence, the momentum equation is modified as

$$\rho \frac{\mathrm{D}\boldsymbol{u}}{\mathrm{D}t} = \boldsymbol{\nabla} \cdot \boldsymbol{T} + A\boldsymbol{u}, \tag{33}$$

in which $\boldsymbol{T}$ is the stress tensor and $A$ is the linear forcing term. The difficulty of this formulation is that the rate of energy supply, and dissipation will not be steady variables for a constant $A$. As a result, implementation of Eq. (33) with a constant $A$ produces a time-dependent $\tau_\eta$ with fluctuations persisting over long periods. These fluctuations have a slow dynamics with an integral time scale that is in the order of hundreds of $\overline{\tau_\eta}$. Since $\tau_\eta$ is directly related to the Stokes number of particles, a correct estimate of St relies on computing $\tau_\eta$ such that conditions are statistically converged. However, the long integral time scale of $\tau_\eta$ inhibits its accurate computation through a reasonable period of ensemble averaging.

To prevent variation of global turbulence statistics several remedies have been explored [32]. Here we developed a method that dynamically changes the linear forcing term $A$ at each time step using

$$A^t = A\left\{1 + \tanh\left[k\left(\frac{\tau_\eta^t}{\tau_\eta} - 1\right)\right]\right\}, \tag{34}$$

in which $A$ is a baseline estimate that is computed from the target Kolmogorov time scale $\tau_\eta$, $A^t$ is dynamically changed forcing term that is implemented in the right-hand-side of Eq. (33), $\tau_\eta^t$ is the instantaneously measured Kolmogorov time scale throughout the simulation, and $k$ is a dimensionless control gain. This method is specifically designed to prevent variation of $\tau_\eta$ throughout the simulation. As shown in Fig. 2, depending on the deviation of $\tau_\eta^t$ from the target value, $A^t$ is

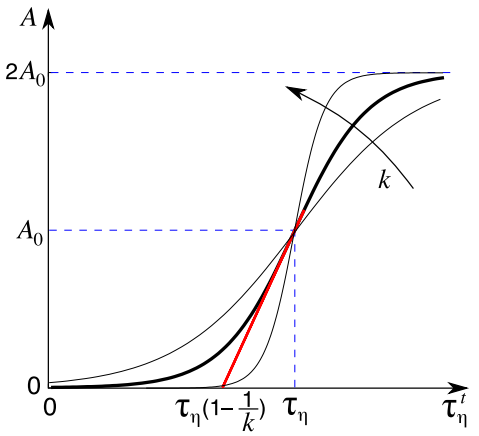


FIG. 2. The dynamic adjustment of the linear forcing coefficient $A^t$ based on the measured $\tau_\eta^t$ using Eq. (34).

increased or decreased with a slope of $kA/\tau_\eta$. For a given box size $L$ and fluid kinematic viscosity $\nu$, we choose $A = \nu^{1/3}L^{-2/3}\tau_\eta^{-2/3}$. This choice produces $\mathrm{Re}_\lambda \approx \sqrt{15}/(3A\tau_\eta)$.

Implementation of Eq. (34) limits the relative error in controlled $\tau_\eta^t$ to a value that scales as $k^{-1}$. As shown in Fig. 3, which is obtained from a simulation at $\mathrm{Re}_\lambda = 26$, controlling $A^t$ reduces $\sqrt{\overline{(\tau_\eta^t/\tau_\eta - 1)^2}}$ from 10% to less than 0.2%. The simulation reported in the following sections is performed at $\mathrm{Re}_\lambda = 100$ with $k = 100$. In this simulation, the maximum deviation of $\tau_\eta^t$ from the target Kolmogorov time scale is 0.3%.

The second aspect of these simulations that requires close attention is the interpolation scheme for computing quantities at the location of particles from the Eulerian grid. To accurately compute the compressibility of particle velocity field, it is essential to have an interpolation scheme that translates the incompressibility condition that is imposed on the Eulerian field to the Lagrangian field. In the

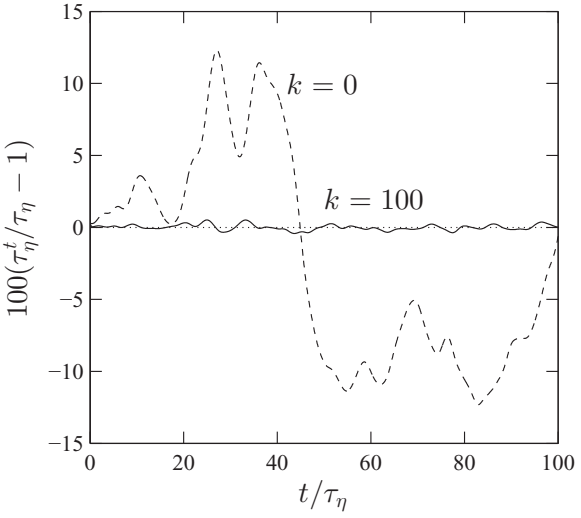


FIG. 3. Deviation of the instantaneous Kolmogorov time scale $\tau_\eta^t$ from the target $\tau_\eta$ in percent over the entire simulation history for controlled $A^t$ with $k = 100$ (solid line) and uncontrolled $A^t$ with $k = 0$ (dashed line).

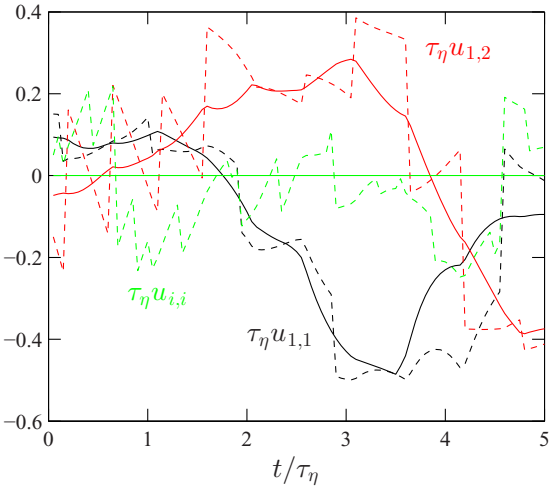


FIG. 4. The Lagrangian velocity gradients as a function of time for an arbitrary particle interpolated from an Eulerian velocity field. As a particle crosses a cell boundary, a jump is observed in the velocity gradients due to the finite support of the interpolation scheme (dashed lines). This issue, originally caused by performing interpolation and then differentiation, is resolved by first creating a spatially consistent $C^0$ continuous field for the velocity gradient and then performing the Lagrangian interpolation (solid lines).

other words, $u_{i,i}(X(t);t)$ evaluated at the location of particles must be zero for incompressible flows. An interpolation scheme with an improper design will not satisfy this condition. The second issue that may arise in this context is a discontinuity in the interpolated velocity gradients along the trajectory of a particle as it crosses over Eulerian cell boundaries (Fig. 4). For example, this issue becomes apparent in the case of constructing velocity gradients from the interpolated velocities through finite differencing. Note that increasing the order of interpolation scheme (for a finite interpolation stencil) does not resolve this problem.

To prevent these two issues, we compute the velocity gradient on the Eulerian grid prior to the Eulerian-to-Lagrangian interpolation. More specifically, for a staggered uniform grid and a second order central differencing, $u_{i,i}$ is computed on the cell center based on the velocities on the faces of the cell. For $u_{i,j}$ and $i \neq j$, gradients are computed on the cell faces from the adjacent cells velocities (e.g., cell $I+1$ is computed based on the cells $I$ and $I+2$). This Eulerian representation of $u_{i,j}$ is then fed into a trilinear interpolation scheme that respects the location of Eulerian quantities on the grid while computing $u_{i,j}$ at the location of particles. The combination of these two steps produces a $C^0$ continuous velocity gradient as a function of time that automatically satisfies the incompressibility condition (Fig. 4).

## IV. ANALYSIS OF THE LAGRANGIAN AUTOCOVARIANCE FUNCTIONS

In this section the autocovariance functions, defined in Eqs. (30) and (31), are computed for a HIT flow. DNS of a triply periodic incompressible flow at $\mathrm{Re}_\lambda = 100$ was performed using a $256^3$ numerical grid. Turbulence was maintained using a time-varying linear forcing term [Eq. (34)]. Equation (1) was solved for particles with $\mathrm{St} = 2^p$, $p \in \{-4, \ldots, 4\}$. At each Stokes number, $10^5$ randomly seeded particles were simulated for several large eddy turnover time to allow development of clusters. Starting from this time-evolved distribution, the velocity gradient tensor was recorded at the position of each particle for $200\tau_\eta$ with $0.1\tau_\eta$ intervals. The scheme described in Sec. III was employed for proper interpolation of the velocity gradients from the Eulerian grid to the location of particles. Having $u_{i,j}$ as a function of time, the autocovariance functions were computed based on Eq. (30) at each St. For ensemble averaging, denoted by $\langle \bullet \rangle$ hereafter, this process is repeated for all

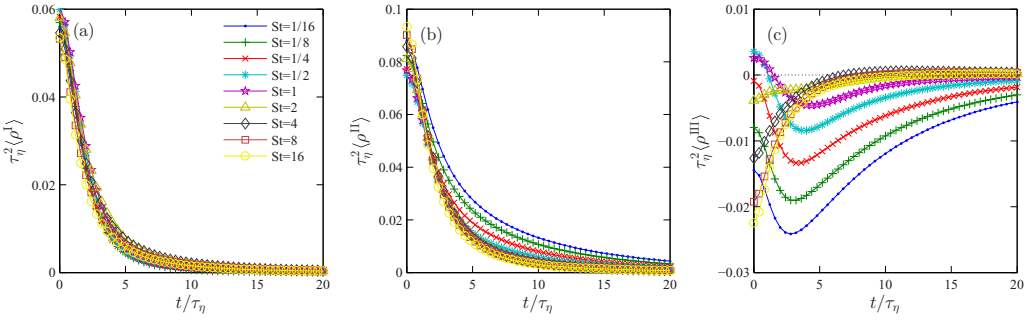


FIG. 5. The ensemble-averaged Lagrangian autocovariance functions (a) $\langle\rho^{\mathrm{I}}\rangle$, (b) $\langle\rho^{\mathrm{II}}\rangle$, and (c) $\langle\rho^{\mathrm{III}}\rangle$ defined in Eq. (30) at different Stokes numbers.

particles ($10^5$ samples at each St). The number of particles and integration period are verified to be sufficient for achieving statistical convergence. The results of these calculations are shown in Fig. 5.

To analyze the trends observed in Fig. 5, we investigate the behavior of each autocovariance function on a set of canonical flows. For this purpose, we consider a flow through a corner, a shear flow, a forced vortex, and a free vortex (Fig. 6). The simple form of the velocity gradient in these flows allows analytical computation of their corresponding autocovariance functions. Employing these analytical forms to explain the behavior of the autocovariance functions in the HIT flow is by no means conclusive and solely conducted for a qualitative understanding of the observed trends. A more conclusive study would require assessment of the likelihood of exposure of particles to different flow features, which must incorporate the dependence on St, as well as a more comprehensive range of canonical flows that may occur in a three-dimensional flow [33].

We first consider flow through a corner or toward a stagnation point, in which $\boldsymbol{u} \equiv [x_1, x_2, -2x_3]A$. In this case, $u_{i,j}$ is zero for $i \neq j$, $A$ for $i = j = 1$ or 2, and $-2A$ for $i = j = 3$. As a result, this canonical flow contributes only to $\rho^{\mathrm{I}}$. Although the trajectory of particles varies with the Stokes number, the gradients are uniform in the entire domain, producing $\rho^{\mathrm{I}} = 2A^2$, which is independent of St. The independence is relatively consistent with Fig. 5(a), in which $\rho^{\mathrm{I}}(t)$ remains unchanged

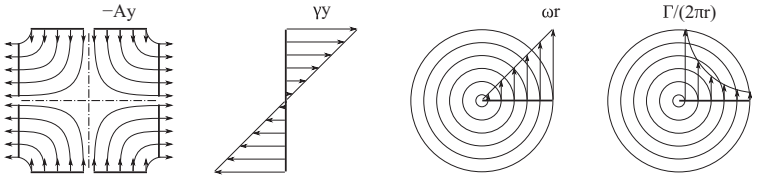


| | (I) | (II) | (III) | (IV) |
|---|---|---|---|---|
| $\rho^{\mathrm{I}}$ | ✓ | — | — | ✓ |
| $\rho^{\mathrm{II}}$ | — | ✓ | ✓ | ✓ |
| $\rho^{\mathrm{III}}$ | — | — | ✓ | ✓ |
| $\rho^{\Omega}$ | — | ✓ | ✓ | — |
| $\rho^{\mathrm{S}}$ | ✓ | ✓ | — | ✓ |
| $\rho^{\mathrm{Q}}$ | ✓ | — | ✓ | ✓ |

FIG. 6. The schematic of four canonical flows and their effect on various autocovariance functions.

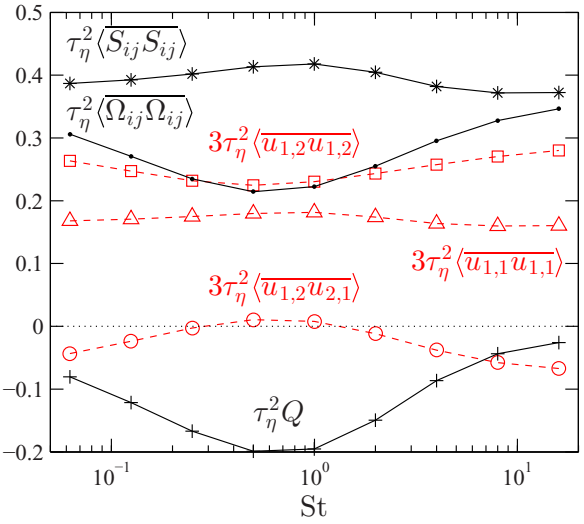


FIG. 7. The ensemble-averaged velocity gradients $\overline{u_{1,1}u_{1,1}}$ (dashed triangles), $\overline{u_{1,2}u_{1,2}}$ (dashed squares), $\overline{u_{1,2}u_{2,1}}$ (dashed circles), rotation rate (solid dots), strain rate (solid stars), and $Q$ criterion (solid plus) as a function of St. Note $Q = -\overline{u_{i,j}u_{j,i}} = \|\boldsymbol{\Omega}\|^2 - \|\boldsymbol{S}\|^2$ is two times the traditional definition of the $Q$ criterion [26], here defined for inertial particles in a Lagrangian framework. Each point in this plot corresponds to an autocorrelation function at zero-time separation, which is the intercept of individual curves in Figs. 5 and 8.

as St is increased from 1/16 to 16. For $t \to \infty$, $u_{i,j}(t')$ becomes uncorrelated with $u_{i,j}(t+t')$, and hence all functions decay to zero. $\rho^{\mathrm{I}}$, however, has the fastest decay rate (shortest integral time scale) among the three functions, indicating that particles travel relatively fast through straining regions of the flow.

Next, we consider a pure shear flow with $\boldsymbol{u} \equiv [x_2,0,0]\gamma$. In this case, only $u_{1,2}$ is nonzero, producing $\rho^{\mathrm{II}} = \gamma^2/6$ and $\rho^{\mathrm{I}} = \rho^{\mathrm{III}} = 0$. The particle trajectories in this flow are straight lines in the $x_1$ direction and independent of St. However, $\rho^{\mathrm{II}}(t)$ in Fig. 5(b) varies as St changes. Apart from the shear flow, $\rho^{\mathrm{II}}$ is affected by the forced and free vortex flows as well (Fig. 6). As discussed next, the contribution of a forced vortex to $\rho^{\mathrm{II}}$ is St dependent. Attributing the dependence of $\rho^{\mathrm{II}}$ on St to the forced vortex, the remaining portion of $\rho^{\mathrm{II}}$ may be attributed to the contribution of regions that are analogous to the shear flow. Comparing the scales of the plots in Fig. 5, the St-independent portion of $\rho^{\mathrm{II}}$ is notable, suggesting significant exposure of particles to shear in HIT.

The third canonical flow is a forced vortex with $\boldsymbol{u} \equiv [-x_2,x_1,0]\omega$. For this flow, $\rho^{\mathrm{I}} = 0$, $\rho^{\mathrm{III}} = -\omega^2/3$, and $\rho^{\mathrm{II}} = \omega^2/3$. The trajectory of particles in this flow scales as $r \propto \exp(ct)$, in which $r$ is the distance from the vortex core and $c(\tau,\omega)$ is the solution to $(\tau c + 1)^2 = \tau c + \tau\omega$. As a result, the residence time of particles in the core of a forced vortex depends on St. This dependence and also $\rho^{\mathrm{II}} = -\rho^{\mathrm{III}}$ may explain the trend of these two autocovariance functions versus St at $t \ll \tau_\eta$ (reproduced in Fig. 7). As St is increased monotonically, $\rho^{\mathrm{II}}(0) = \overline{u_{1,2}u_{1,2}}$ is decreased and increased while $\rho^{\mathrm{III}}(t=0) = \overline{u_{1,2}u_{2,1}}$ is increased and decreased with a similar amplitude. $\overline{u_{1,2}u_{1,2}}$, which is $\propto\omega^2$ in a forced vortex, is minimized at $\mathrm{St} = O(1)$, confirming the notion that particles in strong clustering regimes of St are repelled from the vortices.

Last, we consider a free vortex with $\boldsymbol{u} = [-x_2,x_1,0]\Gamma/(2\pi r^2)$ in which $r^2 = x_1^2 + x_2^2 + x_3^2$ is the distance from the center of the vortex. In this flow $u_{1,2} = u_{2,1} = c\cos(2ct)$ and $u_{1,1} = c\sin(2ct)$, in which $c = \Gamma/(2\pi r^2)$, producing nonzero $\rho^{\mathrm{I}}$, $\rho^{\mathrm{II}}$, and $\rho^{\mathrm{III}}$. Computing the exact value of the autocovariance functions requires finding $r(t)$, a nonlinear function that depends on the dimensionless parameter $\Gamma\tau/r(t=0)$. However, $r$ is almost constant for $t \ll \tau$ and $r \propto t^{1/4}$ for $t \gg \tau$. Neglecting the dependence of $r$ on $t$, it can be shown $\rho^{\mathrm{I}}/2 = \rho^{\mathrm{II}} = \rho^{\mathrm{III}} = c^2/6\cos(2ct)$. This relationship provides an explanation for the decrease and increase of $\rho^{\mathrm{III}}$ in time for $\mathrm{St} \leqslant 1$ [Fig. 5(c)]. Based on

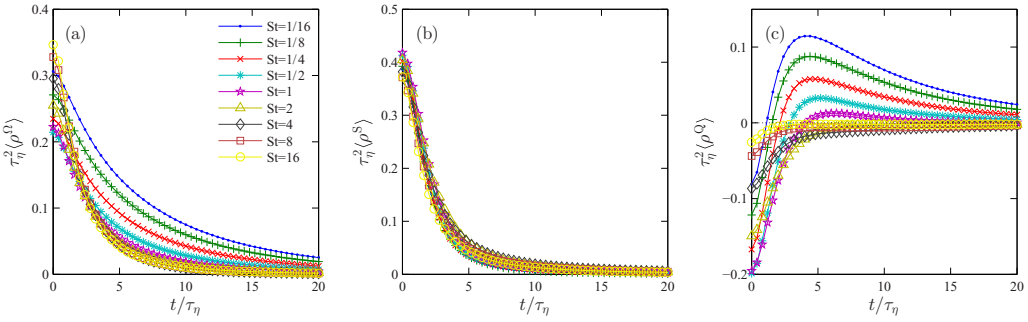


FIG. 8. The ensemble-averaged Lagrangian (a) rotation-rate and (b) strains-rate autocovariance functions and (c) their difference versus time at different Stokes numbers.

this relationship, $\rho^{\mathrm{III}}(0) - \min_t(\rho^{\mathrm{III}}(t)) \propto c^2$ and $\mathrm{argmin}_t(\rho^{\mathrm{III}}(t)) \propto c^{-1}$. This relation is consistent with the variation of $\rho^{\mathrm{III}}$ for $t < 5\tau_\eta$ and $\mathrm{St} \leqslant 1$ in which a larger change in amplitude is associated with a shorter time at which the minimum of $\rho^{\mathrm{III}}$ occurs [Fig. 5(c)]. As opposed to $\rho^{\mathrm{III}}$, $\rho^{\mathrm{I}}$ and $\rho^{\mathrm{II}}$ are apparently unaffected by the free vortices and follow a monotonic trend. An explanation for this behavior is the influence of other canonical flows with larger relative contributions on the latter two functions. To obtain a scale for the relative magnitude of these contributions, note the larger amplitude of $\rho^{\mathrm{I}}$ and $\rho^{\mathrm{II}}$ in comparison with $\rho^{\mathrm{III}}$ (Fig. 5).

The calculated autocovariance functions can be combined to obtain strain- and rotation-rate autocovariance functions according to Eq. (31) (Figs. 7 and 8). The effect of aforementioned canonical flows on these functions can also be examined by summing their corresponding contribution on $\rho^{\mathrm{I}}$, $\rho^{\mathrm{II}}$, and $\rho^{\mathrm{III}}$ (Fig. 6). In Fig. 8(b) $\rho^{\mathrm{S}}$ is relatively independent of St despite the fact that $\rho^{\mathrm{II}}$ and $\rho^{\mathrm{III}}$ vary significantly as St changes. This independence shows that the variation of $\rho^{\mathrm{II}}$ and $\rho^{\mathrm{III}}$ versus St are opposite, a behavior that specifically holds in a forced vortex as was shown earlier. These opposite variations, on the other hand, are amplified in $\rho^{\Omega}$, producing a marked dependence on St [Fig. 8(a)]. Among those considered, $\rho^{\Omega}$ is interestingly the only function that is not sensitive to a free vortex (Fig. 6). $\rho^{\mathrm{Q}}$ captures the effect of all the considered canonical flows but the shear flow. Having $\rho^{\mathrm{Q}} = 0$ for a shear flow is an expected outcome because $\mathcal{C}$, which is a function of $\tilde{\rho}^{\mathrm{Q}}$, must be zero in a pure shear flow (no particle clustering is expected in a pure shear flow).

At the limit of very large Stokes numbers, particles are not responsive to the velocity fluctuations and follow a trajectory that is uncorrelated with the flow. As a result, the Lagrangian statistics at this limit converge to the Eulerian statistics, which are by definition obtained from a fixed location in space that is uncorrelated with the flow. Additionally, the Eulerian strain- and rotation-rate autocovariance functions are equal on a periodic domain. Therefore, the Lagrangian strain- and rotation-rate autocovariance functions, i.e., $\rho^{\mathrm{S}}$ and $\rho^{\Omega}$, converge to the same value at the limit of large St (Fig. 8). This leads to $\rho^{\mathrm{Q}} \to 0$ at the limit of large St. Moreover, since $\rho^{\mathrm{S}}$ is relatively independent of the Stokes number, one may conclude that the trajectory of inertial particles is poorly correlated with the flow strain-rate field. This is not the case, however, with the flow rotation-rate field as $\rho^{\Omega}$ varies significantly versus St [Fig. 8(a)]. $\rho^{\mathrm{Q}}$ for $\mathrm{St} \leqslant O(1)$ undergoes an increasing-decreasing trend in time, which is a consequence of the similar behavior in $\rho^{\mathrm{III}}$. Attributing this trend to the flow regions that behave similar to a free vortex, one can explain the change in the amplitude and phase of this oscillation as a function of St by using the expression derived above along with an estimate of the residence time of particles in a free vortex.

Some of the results of this section, specifically those included in Fig. 7, are discussed in more detail in Refs. [29,34]. From Fig. 7, the extremum of $\tau_\eta^2 Q$ is approximately $-0.2$, which is consistent with the previously reported 0.2 for the maximum of $\tau_\eta^2\overline{(\|\boldsymbol{S}\|^2 - \|\boldsymbol{\Omega}\|^2)} = -\tau_\eta^2 Q$ [34]. The agreement between the two studies indicates that $Q$ is fairly insensitive to Reynolds number, as the two studies

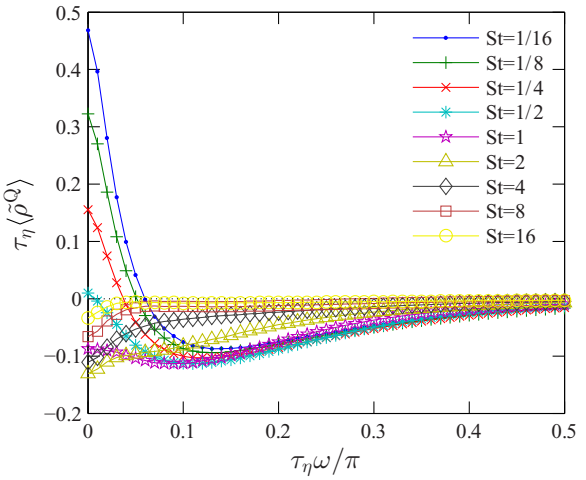


FIG. 9. The Fourier transformation of the autocovariance of the second invariant of the velocity gradient tensor, $\langle\tilde{\rho}^{Q}\rangle$, computed along the trajectory of particles with different Stokes number. Note $\tau_\eta\langle\tilde{\rho}^{Q}(\tau_\eta\omega \ll 1)\rangle \propto 1/\mathrm{St}$ as $\mathrm{St} \to \infty$. Error bars (not shown) are of $O(10^{-4})$.

consider simulations at $\mathrm{Re}_\lambda = 100$ and 60.5. Based on the discrete set of investigated Stokes numbers in these two studies, the Stokes number at which the extremum of $Q$ occurs is 0.5 (present) and 0.64 [34]. A precise assessment of the location of the extremum would require a more refined parameter space.

Taking the Fourier transformation of $\rho^{Q}$ in Fig. 8(c), $\tilde{\rho}^{Q}$ is computed and shown in Fig. 9. A biased sampling of strain- and rotation-rate-rich regions of the flow by inertial particles produces a nonzero $\tilde{\rho}^{Q}$. This figure also confirms that particles with $\mathrm{St} < 1$ tend to follow slow vortical features ($\tilde{\rho}^{Q} > 0$ at $\tau_\eta\omega \ll 1$ and $\mathrm{St} < 1$), while particles with $\mathrm{St} \gg 1$ experience strain and rotation rates equally ($\tau_\eta\tilde{\rho}^{Q} \to 0$ as $\mathrm{St} \to \infty$). Most notably $\tilde{\rho}^{Q}$ is negative across all frequencies for $\mathrm{St} \geqslant O(1)$. Computed $\tilde{\rho}^{Q}$ is employed in the next section to evaluate and validate the present analysis.

## V. NUMERICAL VALIDATION

The objective of this section is to compute the rate of contraction from the analysis that was proposed in Sec. II and validate it using a direct approach. Hence, we first describe a direct method that provides an accurate estimate of the actual rate of contraction. Additionally, we compute the rate of contraction using present [Eq. (28)] and R-M [Eq. (3)] expressions. Finally, we compare the prediction of these two formulations to the direct computations in terms of $\mathcal{C}$ statistics.

A numerical procedure is devised for direct computation of the contraction rate from the DNS. The direct calculation of $\mathcal{C}$ sets a baseline, allowing to validate our analysis in a HIT flow. Visually, the direct calculation of $\mathcal{C}$ involves constructing a cloud by seeding particles randomly distributed on a spherical shell with an infinitesimal diameter. In practice, as clarified below, a cloud can be represented by computing the Lagrangian velocity gradient along the trajectory of a single particle. Computing the exponential rate of change of volume of the cloud over time provides a direct estimate of the rate of contraction. Therefore, an ensemble of clouds provides an estimate for $\langle\mathcal{C}\rangle$.

Individual particles in the cloud experience an infinitesimally different fluid velocity and as a result follow an infinitesimally different path. This differential change leads to the deformation of the cloud over time. Due to the linear spatial variation of the velocities within the cloud, the deformation is linear and can be represented by a $3 \times 3$ tensor in three dimensions. Applying the deformation tensor to a spherical cloud of particles produces an ellipsoid (Fig. 10). The dimensions and directions of the axis of this ellipsoid are directly related to the eigenvalues and eigenvectors of

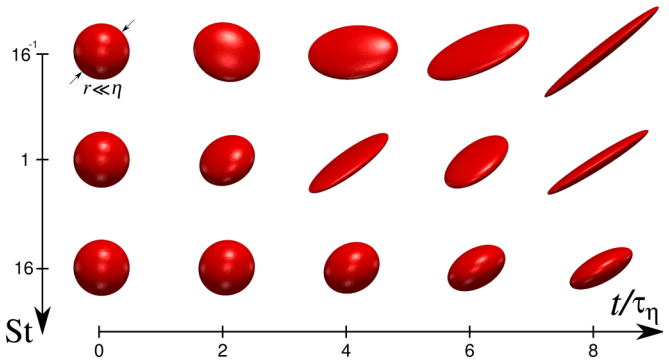


FIG. 10. Deformation of three arbitrary spherical clouds in a HIT flow (particles are not shown). These clouds are constructed using a set of inertial particles initially seeded on a spherical shell. From top to bottom: $\mathrm{St} = 16^{-1}$, 1, and 16. While the cloud with $\mathrm{St} = 16^{-1}$ deforms significantly, its volume remains within 30% of the initial volume. The $\mathrm{St} = 1$ cloud contracts with a twofold decrease in volume. The $\mathrm{St} = 16$ cloud remains almost spherical with a 30% change in volume at $t = 8\tau_\eta$.

the deformation tensor, respectively. For visualization purposes, the deformation of three arbitrary clouds at $\mathrm{St} = \{1/16, 1, 16\}$ that undergo a linear deformation is shown in Fig. 10.

In practice, we compute the time evolution of the deformation tensor from direct integration of Eq. (6) along the trajectory of a single particle. The deformation tensor is formed based on the relative position of three virtual particles to a reference particle. Since $\boldsymbol{r}$ represents the relative position, three columns of the deformation tensor are formed using $\boldsymbol{r}$ associated with the three virtual nonoverlapping particles. The time evolution of the deformation tensor is governed by the motion of these particles and thus by Eq. (6). Integrating this equation requires $u_{i,j}(\boldsymbol{X}(t); t)$ along the trajectory of the cloud, which is extracted from Sec. IV in which the Lagrangian autocovariance functions were computed using the same velocity gradients. Provided that the volume of an infinitesimal cloud is equal to the determinant of its corresponding deformation tensor, the time history of the volume of the cloud is calculated, allowing us to compute the finite-time rate of contraction $\mathcal{C}^t$ based on Eq. (9) (Fig. 11).

Obtaining an accurate estimate of $\mathcal{C}$, defined in Eq. (10), requires integrating Eq. (6) till $t \gg \tau_\eta$. However, due to the exponential rate of contraction or expansion, the system of equations becomes very stiff at a longer time, producing a nearly singular deformation tensor. Having a stiff system prevents an accurate computation of $\mathcal{C}$ by limiting $t$. To circumvent this issue, we integrate an equivalent system of equations for the normalized rate of change of volume, computed as the ratio of the rate of change of volume by the volume, which remains well-conditioned regardless of the integration period. With this change of variables, $\mathcal{C}^t$ is computed for the entire sampling period of $u_{i,j}$, i.e., $200\tau_\eta$. Additionally, the initial condition on the deformation tensor, which is an identity matrix in our computations, affects $\mathcal{C}^t$ at $t = 200\tau_\eta$. To reduce this effect, we repeat the integration for 10 cycles, using the solution at the end of each cycle as the initial condition for the next. Hence, integration is continued for $2000\tau_\eta$ and $\mathcal{C}$ is set to $\mathcal{C}^t$ at $t = 2000\tau_\eta$. This procedure ensures that reported $\mathcal{C}$ is minimally influenced by the initial condition and is time-independent. By repeating these computations for all the available particles ($10^5$ samples that corresponds to $10^5$ clouds at each St), the PDF of $\mathcal{C}$ is constructed and shown in Fig. 12.

The results of the direct computation of $\mathcal{C}$, described above, along with the theoretically predicted $\mathcal{C}$ are shown in Fig. 12. The numerical procedure for computing PDFs of the theoretically computed $\mathcal{C}$ starts from the same data set as the direct computation. $\rho^Q$ is computed from Eq. (29) for every individual particle, representing a cloud or a sample, using the time history of $u_{i,j}$ along the particle trajectory. $Q = \rho^Q(0)$ and $\tilde{\rho}^Q$ is then computed and substituted in Eqs. (3) and (28), respectively, to obtain one sample point of the corresponding PDFs in Fig. 12. Note the linearity of Eqs. (3) and (28)

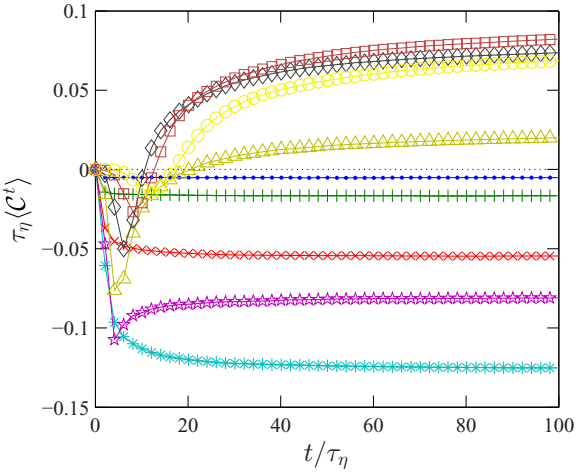


FIG. 11. The ensemble-averaged finite-time contraction rate $\langle\mathcal{C}^t\rangle$ at different St. To ensure a fully stationary condition when computing $\mathcal{C}$ from $\mathcal{C}^t$, integration is continued to $2000\tau_\eta$ (only $t \leqslant 100\tau_\eta$ is shown here). For symbols, see Fig. 9.

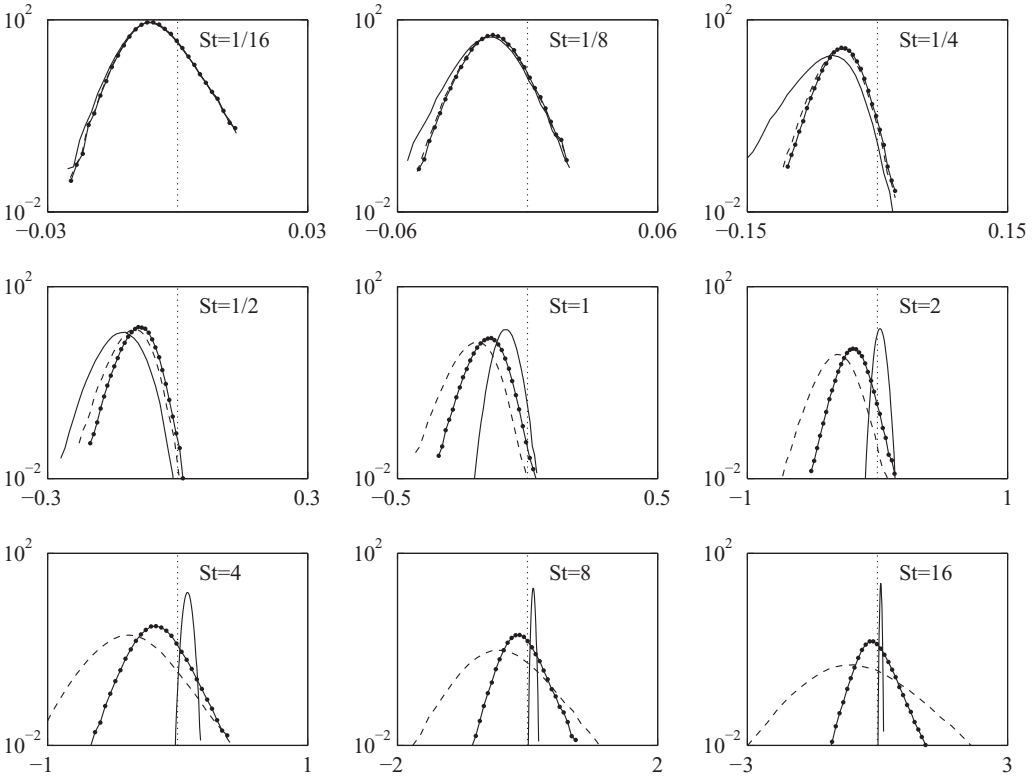


FIG. 12. The PDF of the rate of contraction $\tau_\eta\mathcal{C}^t$ for different Stokes numbers computed by the direct integration of Eq. (6) (solid), using the present analysis, or Eq. (28) (solid dotted), and using R-M or Eq. (3) (dashed). Note that the spread of these PDF varies depending on the sampling period $t$, which is $200\tau_\eta$ in this case.

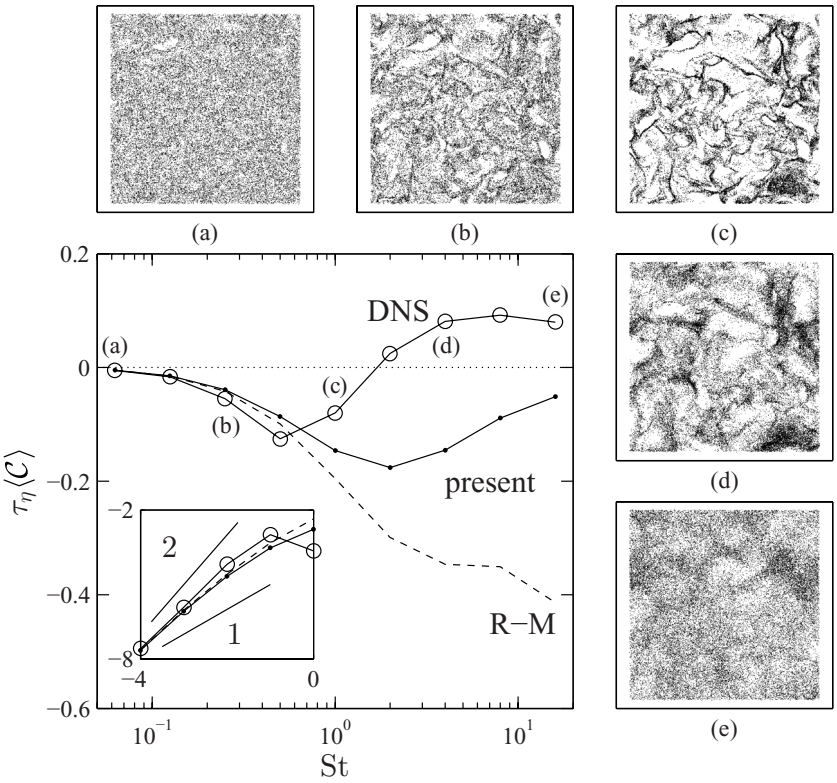


FIG. 13. The theoretically predicted ensemble-averaged rate of contraction $\langle \mathcal{C} \rangle$ using the present analysis that is Eq. (28) (solid dot) and R-M that is Eq. (3) (dashed) at different St. The reference quantities (solid circle) are obtained from the direct computation of $\langle \mathcal{C} \rangle$. Inset: $\log_2(-\mathcal{C})$ versus $\log_2(\mathrm{St})$ for $\mathrm{St} \leqslant 1$. Lines with a slope of 1 and 2 are shown for reference. To visualize clustering, particles are shown in a slab of size $300\eta \times 300\eta \times 10\eta$ for $\mathrm{St} = 16^{-1}$ (a), $4^{-1}$ (b), 1 (c), 4 (d), 16 (e).

with respect to $Q$ and $\tilde{\rho}^{\mathrm{Q}}$ allows one to directly compute the mean of these PDFs from the results of Sec. IV.

Taking the direct calculation of $\mathcal{C}$ as the reference, the present analysis offers an improvement over R-M. As we discussed in the derivation of Eq. (32) and now is confirmed by this figure, the prediction of the present analysis converges to that of R-M at the limit of small St. Additionally, the PDF of both analyses collapses with that of the direct calculations, confirming the accuracy of both formulas in the limit of small St. The accuracy of R-M at this limit has also been shown previously by comparing it against the exact solution of Eq. (6) in straining and vortical flows [34]. In general, the prediction of the present analysis is closer to R-M than the reference values. While both analyses are erroneous at large St, the error of the present analysis is smaller than that of R-M. For a closer comparison, the mean of these PDFs is plotted in Fig. 13.

The analytically computed $\langle \mathcal{C} \rangle$ can be compared to the direct computations at two limits of $\mathrm{St} < 1$ and $\mathrm{St} > 1$. For $\mathrm{St} < 1$, $\langle \mathcal{C} \rangle < 0$ and contraction dominates expansion. The rate of contraction increase as St increases, explaining the stronger clustering of particles with $\mathrm{St} = O(1)$. $\tau_\eta \min_{\mathrm{St} \leqslant 1} \langle \mathcal{C} \rangle \approx -1/8$, which occurs at $\mathrm{St} = 1/2$ on the discrete set of investigated St. In the regime of $\mathrm{St} \ll 1$, $\langle \mathcal{C} \rangle$ follows a power law with $-\tau_\eta \langle \mathcal{C} \rangle \propto \mathrm{St}^\alpha$, in which $\alpha \approx 1.7$ (inset of Fig. 13). This power-law behavior is well established in the literature for the low Stokes numbers. For a synthetic flow generated from random Fourier modes, $\alpha$ has been reported to be 2 [16]. This minor difference can be ascribed to the use of

a synthetic flow as opposed to HIT in the previous study. The slope of 1.7 in our computation is a result of $\lim_{\mathrm{St}\to 0} -\tau_\eta^2 Q \propto \mathrm{St}^{0.7}$ (Fig. 7).

For $\mathrm{St} > 1$, $\langle \mathcal{C} \rangle$ increases and becomes positive, indicating the dominance of expansion over contraction [1,16]. At a Stokes number between 1 and 2, the mean rates of expansion and contraction become equal. Although $\langle \mathcal{C} \rangle = 0$ at this St, individual clouds still experience a significant change in volume over time and particles form distinct clusters [see Figs. 13(c) and 13(d)]. Neither of two analyses captures the positive value of $\langle \mathcal{C} \rangle$ at large St. However, the present analysis remains bounded by predicting an extremum for $\langle \mathcal{C} \rangle$ at $\mathrm{St} = O(1)$ as opposed to the prediction of R-M that grows linearly within the investigated range of St. For $\mathrm{St} \gg 1$, the present analysis predicts $\langle \mathcal{C} \rangle \propto \mathrm{St}^{-1}$, which is a result of $\langle \tilde{\rho}^{\mathrm{Q}}(\tau_\eta \omega \ll 1) \rangle \propto \mathrm{St}^{-1}$ (Fig. 9). The error in the predictions of the present analysis can be primarily attributed to the assumption $|\lambda\tau| \ll 1$ in Eq. (12), which is not satisfied well at larger St ($|\lambda\tau| > 0.1$ for $\mathrm{St} \geqslant 4$). The effect of this assumption on the accuracy of the predictions can be observed even at $\mathrm{St} = 1/4$. Considering $\mathrm{St} = 1/4$ case in Fig. 12, the largest deviation from the reference values occurs on the left tail, where $|\mathcal{C}^t|$ and consequently $|\lambda\tau|$ is the largest. The location of this discrepancy underscores the importance of the $|\lambda\tau| \ll 1$ assumption in the validity of the present analysis. This assumption must be relaxed in future studies to improve predictions at large St. Despite this discrepancy, Eq. (28) captures the nonmonotonic behavior of $\langle \mathcal{C} \rangle$ with a maximum rate of contraction 40% larger than that of the direct computations.

As confirmed by the patterns observed in Figs. 13(a) and 13(e), particles in the regimes at which $\mathcal{C} < 0$ and $\mathcal{C} > 0$ behave differently. In mathematical terms, the volume of the region occupied by particles would increase or decrease in time depending on the sign of $\mathcal{C}$. In physical terms, this change of volume has been described as mixing ($\mathcal{C} > 0$) and demixing ($\mathcal{C} < 0$) [16]. For particles that undergo demixing, ridges with high particle concentration is formed from a distribution that is initially homogeneous [Fig. 13(c)]. In a reversed time frame this behavior is the same as injecting a dye in the ridges and observing its diffusion to a homogeneous mixture as time passes. On the other hand, particles with high St undergo mixing with $\mathcal{C} > 0$. For an observer who is unable to discern fine-scale features of the flow, particle mixing at this limit is similar to mixing of a dye in a turbulent flow as they both appear to lead to a homogenized mixture. However, in the absence of molecular diffusion, there is an important difference between the two processes. While $\mathcal{C} > 0$ for large St particles, $\mathcal{C} = 0$ for a dye. When a drop of dye is injected into a turbulent flow with no molecular diffusion, the interface deforms to a very complex and twisted geometry. Nevertheless, the interface remains sharp, and the volume occupied by the dye remains constant in time. This is not the case, however, with the large St particles. If a set of large St particles are introduced into a small enclosed region of a turbulent flow, the volume associated with that region will increase exponentially as the time progresses. In this case, an initially sharp interface will diffuse over time due to the nonuniqueness of particle velocities at a given point in space.

It is important to note that the above description is given for the average behavior of the particles. The clouds of particles with large St experience $\mathcal{C}^t < 0$ intermittently as they travel through different regions of the flow. The opposite is also true for small St particles. The PDF of $\mathcal{C}^t$ crosses zero at all Stokes numbers, although not observed clearly in Fig. 12 due to the long sampling period that has reduced the spread of PDFs. Intermittent demixing of large St particles is also confirmed by Fig. 13(e), which shows regions of higher concentration that are significantly diffused.

The PDFs of $\mathcal{C}^t$ appears to be Gaussian in Fig. 12. To closely examine this observation, all the PDFs obtained from the direct computations are shifted by their mean, normalized by their standard deviation, and plotted in Fig. 14. The standardized PDFs at large St match well with the parabolic function that represents a Gaussian distribution. For the Stokes numbers close to 1/4, a negative skewness is observed, showing higher incidents of strong contraction events as compared to strong expansion events (Fig. 14). At the smallest St, the right tail of the PDF is approximately linear, indicative of biased exposure of neutral particles to strong expansion events in HIT. With slight variations, this observation is compatible with the corresponding results obtained from HIT and synthetic flows [16,20,35].

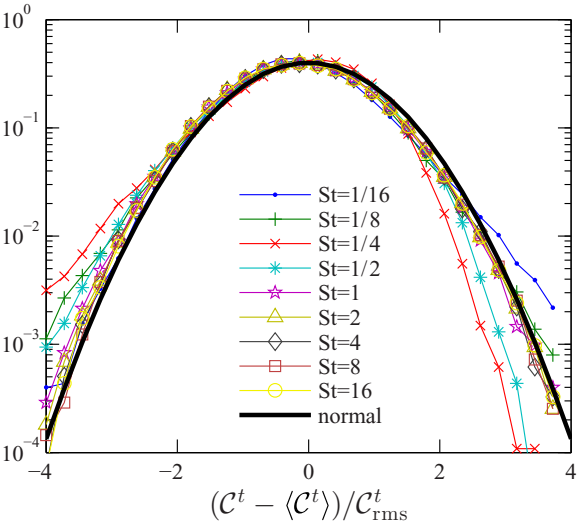


FIG. 14. Standardized PDF of the finite-time rate of contraction $\mathcal{C}^t$ obtained from the direct integration of Eq. (6) at different St. The solid line is a Gaussian distribution, shown as a reference.

The second order statistics of $\mathcal{C}^t$, defined as

$$\mathcal{C}^t_{\rm rms} = \sqrt{\langle(\mathcal{C}^t - \langle\mathcal{C}^t\rangle)^2\rangle}, \tag{35}$$

is a function that depends on the sampling period $t$. For $t$ larger than the integral time scale of $\mathcal{C}$, $\mathcal{C}^t_{\rm rms}$ scales as $t^{-1/2}$ [20]. Thus, $\sqrt{\tau_\eta t}\mathcal{C}^t_{\rm rms}$ is computed as a time-independent quantity and plotted in Fig. 15. This quantity is directly related to the compression diffusion coefficient $D(\infty)$, defined in Ref. [20], via $\sqrt{\tau_\eta t}\mathcal{C}^t_{\rm rms} = \sqrt{2\tau_\eta D(\infty)}$ and is mainly governed by the turbulence intermittency. Considering the directly computed quantities in Figs. 13 and 15, the extremum of $\mathcal{C}_{\rm rms}$ and $\langle\mathcal{C}\rangle$ occurs

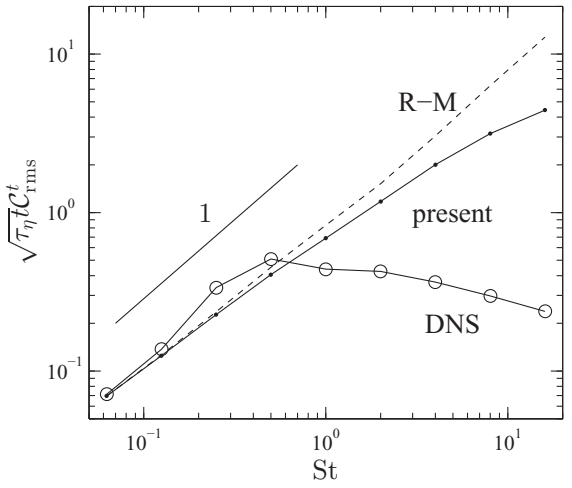


FIG. 15. The standard deviation of the rate of contraction $\mathcal{C}^t_{\rm rms}$ using the present analysis (solid dot), R-M (dashed), and the direct computations (solid circle) as a function of St. To make values independent of $t$, $\mathcal{C}^t_{\rm rms}$ is multiplied by $\sqrt{t}$.

at the same St. The prediction accuracy of the two analyses in terms of $\mathcal{C}_{\rm rms}$ is analogous to $\langle\mathcal{C}\rangle$. Both models agree well with the direct computations at the limit of small St and deviate from it as St increases. The error associated with the present analysis, however, is slightly smaller than R-M at large St. The prediction of R-M scales as $\sqrt{\tau_\eta t}\mathcal{C}^t_{\rm rms}(\mathrm{St}) \propto \mathrm{St}$, while the present analysis produces slightly smaller values for $\mathrm{St} \geqslant 1$.

The nonmonotonic prediction of $\langle\mathcal{C}(\mathrm{St})\rangle$ by our analysis is in agreement with previous investigations that have characterized clustering via other indices, yet consistently finding maximum clustering at $\mathrm{St} = O(1)$ [3,10,14,28]. The outcome of this study may have implications in developing two-particle models for large-eddy simulation of particle-laden turbulent flows [36] and an equilibrium Eulerian method for affordable computation of the particle velocity field [29,34]. Additionally, one may directly relate the contraction rate of clouds of particles $\mathcal{C}$ to

$$d_{\rm L} = 3 - (\lambda_1 + \lambda_2 + \lambda_3)/\lambda_3 = 3 - \mathcal{C}/\lambda_3, \tag{36}$$

which is the Lyapunov dimension introduced by Kaplan and York [37]. In this equation, which is valid for a three-dimensional flow, exponents follow a descending order such that $\lambda_3 < \lambda_2 < \lambda_1$. Since in three dimensions $\lambda_3 < 0$ [35], $d_{\rm L}$ is smaller than the number of spatial dimensions for $\mathcal{C} < 0$. At this limit in which particle clusters are fractals, $d_{\rm L}$ represents the dimension of the space that contains a homogeneous distribution of particles. By estimating $\lambda_3$, one may employ the result of this analysis to estimate $d_{\rm L}$. As we discussed in Sec. I, this dimension can also be related to the particle concentration field statistics through $\zeta$.

## VI. CONCLUSIONS

In summary, we derived an asymptotic solution [Eq. (28)] for the rate of contraction of the cloud of inertial particles, defined as the summation of the Lyapunov exponents in three principal directions, in regimes relevant to particle-laden turbulent flows. The analytical model that we derived predicts a maximum rate of contraction at $\mathrm{St} = O(1)$ and diminishing rates of contraction as $\mathrm{St} \to 0$ or $\infty$. No adjustable parameters were employed in our model to predict this nonmonotonic variation versus the Stokes number. The developed model reproduces R-M, which is a previously established result [25,29], at small St and offers a first order correction to it at large St. Similarly to R-M, our analysis accounts for the background flow through $\tilde{\rho}^{\rm Q}$, which is the Fourier transformation of the autocovariance of the second invariant of velocity gradient tensor. We showed that $\tilde{\rho}^{\rm Q}$, which is computed along the trajectory of particles, varies significantly versus the Stokes number. The Lagrangian autocovariance functions, which are closely related to $\tilde{\rho}^{\rm Q}$, were computed at different St for a HIT flow and were analyzed by a set of canonical flows with established behavior. From these results, the first and second order statistics of the rate of contraction was computed using our analysis and a direct numerical approach. Comparing our analysis and the direct computations showed a good agreement between the two at the limit of small St. For higher St, despite the fact that the predictions of our analysis are not in full agreement with the direct computations, it still offers an improvement over R-M. The inaccuracy of the present analysis is primarily attributed to the assumption $|\lambda\tau| \ll 1$, which breaks down at this regime of St. Further studies are required to address this discrepancy by analytically characterizing the behavior of particles with $\mathrm{St} \geqslant O(1)$ in turbulent flows. The developed analysis reveals the contribution of different time scales in turbulence to the clustering phenomenon via $\tilde{\rho}^{\rm Q}(\omega)$. Relaxing the underlying assumptions of the present analysis, namely, those associated with the contribution of small frequencies in Eqs. (21) and (23) and the slow contraction rate in Eq. (12), warrants future studies. Additionally, the extension of the present formulation to compressible and anisotropic turbulent flows remains a subject of future studies.

## ACKNOWLEDGMENTS

We thank Professors Parviz Moin and John Eaton for fruitful discussions. This Material is based upon a study supported by the United States Department of Energy National Nuclear Security

Administration under the Predictive Science Academic Alliance Program 2 (PSAAP2) at Stanford University (Award Number DE-NA0002373-1).

---

[1] J. Bec, Fractal clustering of inertial particles in random flows, Phys. Fluids **15**, L81, (2003).
[2] E. Calzavarini, M. Cencini, D. Lohse, and F. Toschi, Quantifying Turbulence-Induced Segregation of Inertial Particles, Phys. Rev. Lett. **101**, 084504 (2008).
[3] W. C. Reade and L. R. Collins, Effect of preferential concentration on turbulent collision rates, Phys. Fluids **12**, 2530 (2000).
[4] J. K. Eaton and J. R. Fessler, Preferential concentration of particles by turbulence, Int. J. Multiphase Flow **20**, 169 (1994).
[5] S. Balachandar and J. K. Eaton, Turbulent dispersed multiphase flow, Annu. Rev. Fluid Mech. **42**, 111 (2010).
[6] J. R. Fessler, J. D. Kulick, and J. K. Eaton, Preferential concentration of heavy particles in a turbulent channel flow, Phys. Fluids **6**, 3742 (1994).
[7] A. Aliseda, A. Cartellier, F. Hainaux, and J. C. Lasheras, Effect of preferential concentration on the settling velocity of heavy particles in homogeneous isotropic turbulence, J. Fluid Mech. **468**, 77 (2002).
[8] J. P. L. C. Salazar, J. De Jong, L. Cao, S. H. Woodward, H. Meng, and L. R. Collins, Experimental and numerical investigation of inertial particle clustering in isotropic turbulence, J. Fluid Mech. **600**, 245 (2008).
[9] E. W. Saw, R. A. Shaw, S. Ayyalasomayajula, P. Y. Chuang, and A. Gylfason, Inertial Clustering of Particles in High-Reynolds-Number Turbulence, Phys. Rev. Lett. **100**, 214501 (2008).
[10] B. Ray and L. R. Collins, Preferential concentration and relative velocity statistics of inertial particles in Navier-Stokes turbulence with and without filtering, J. Fluid Mech. **680**, 488 (2011).
[11] Y. Tagawa, J. Martínez Mercado, V. N. Prakash, E. Calzavarini, C. Sun, and D. Lohse, Three-dimensional Lagrangian Voronoi analysis for clustering of particles and bubbles in turbulence, J. Fluid Mech. **693**, 201 (2012).
[12] S. Goto and J. C. Vassilicos, Sweep-Stick Mechanism of Heavy Particle Clustering in Fluid Turbulence, Phys. Rev. Lett. **100**, 054503 (2008).
[13] J. Bec, Multifractal concentrations of inertial particles in smooth random flows, J. Fluid Mech. **528**, 255 (2005).
[14] J. Bec, L. Biferale, M. Cencini, A. Lanotte, S. Musacchio, and F. Toschi, Heavy Particle Concentration in Turbulence at Dissipative and Inertial Scales, Phys. Rev. Lett. **98**, 084502 (2007).
[15] K. D. Squires and J. K. Eaton, Preferential concentration of particles by turbulence, Phys. Fluids A: Fluid Dyn. (1989–1993) **3**, 1169 (1991).
[16] R. H. A. Ijzermans, E. Meneguz, and M. W. Reeks, Segregation of particles in incompressible random flows: Singularities, intermittency and random uncorrelated motion, J. Fluid Mech. **653**, 99 (2010).
[17] H. Aref and S. Balachandar, Chaotic advection in a Stokes flow, Phys. Fluids **29**, 3515 (1986).
[18] R. Monchaux, M. Bourgoin, and A. Cartellier, Analyzing preferential concentration and clustering of inertial particles in turbulence, Int. J. Multiphase Flow **40**, 1 (2012).
[19] S. C. Shadden, F. Lekien, and J. E. Marsden, Definition and properties of Lagrangian coherent structures from finite-time Lyapunov exponents in two-dimensional aperiodic flows, Physica D: Nonlinear Phenom. **212**, 271 (2005).
[20] E. Meneguz and M. W. Reeks, Statistical properties of particle segregation in homogeneous isotropic turbulence, J. Fluid Mech. **686**, 338 (2011).
[21] H. G. E. Hentschel and I. Procaccia, The infinite number of generalized dimensions of fractals and strange attractors, Physica D: Nonlinear Phenom. **8**, 435 (1983).
[22] J. Bec, K. Gawedzki, and P. Horvai, Multifractal Clustering in Compressible Flows, Phys. Rev. Lett. **92**, 224501 (2004).

[23] M. Wilkinson, B. Mehlig, and K. Gustavsson, Correlation dimension of inertial particles in random flows, Europhys. Lett. **89**, 50002 (2010).
[24] A. Robinson, On the motion of small particles in a potential field of flow, Comm. Pure Appl. Math. **9**, 69 (1956).
[25] M. R. Maxey, The gravitational settling of aerosol particles in homogeneous turbulence and random flow fields, J. Fluid Mech. **174**, 441 (1987).
[26] J. C. R. Hunt, A. A. Wray, and P. Moin, Eddies stream, and convergence zones in turbulent flows, Center for Turbulence Research CTR-S 88, 1988.
[27] Y. Dubief and F. Delcayre, On coherent-vortex identification in turbulence, J. Turbulence **1**, N11 (2000).
[28] L.-P. Wang and M. R. Maxey, Settling velocity and concentration distribution of heavy particles in homogeneous isotropic turbulence, J. Fluid Mech. **256**, 27 (1993).
[29] S. L. Rani and S. Balachandar, Evaluation of the equilibrium Eulerian approach for the evolution of particle concentration in isotropic turbulence, Int. J. Multiphase Flow **29**, 1793 (2003).
[30] E. Balkovsky, G. Falkovich, and A. Fouxon, Intermittent Distribution of Inertial Particles in Turbulent Flows, Phys. Rev. Lett. **86**, 2790 (2001).
[31] C. Rosales and C. Meneveau, Linear forcing in numerical simulations of isotropic turbulence: Physical space implementations and convergence properties, Phys. Fluids **17**, 095106 (2005).
[32] M. Bassenne, J. Urzay, G. I. Park, and P. Moin, Constant-energetics physical-space forcing methods for improved convergence to homogeneous-isotropic turbulence with application to particle-laden flows, Phys. Fluids (1994–present) **28**, 035114 (2016).
[33] A. E. Perry and M. S. Chong, A description of eddying motions and flow patterns using critical-point concepts, Annu. Rev. Fluid Mech. **19**, 125 (1987).
[34] J. Ferry, S. L. Rani, and S. Balachandar, A locally implicit improvement of the equilibrium Eulerian method, Int. J. Multiphase Flow **29**, 869 (2003).
[35] J. Bec, L. Biferale, G. Boffetta, M. Cencini, S. Musacchio, and F. Toschi, Lyapunov exponents of heavy particles in turbulence, Phys. Fluids **18**, 091702 (2006).
[36] B. Ray and L. R. Collins, Investigation of sub-Kolmogorov inertial particle pair dynamics in turbulence using novel satellite particle simulations, J. Fluid Mech. **720**, 192 (2013).
[37] J. L. Kaplan and J. A. Yorke, Functional differential equations and approximation of fixed points, Lect. Notes Math. **730**, 228 (1979).